Accuracy of a novel photoacoustic-based approach to surgical guidance performed with and without a da Vinci robot

Neeraj Gandhi,[a] Sungmin Kim,[b] Peter Kazanzides,[b] Muyinatu A. Lediju Bell*[c,d]

[a]University of Virginia, Department of Electrical and Computer Engineering, Charlottesville, VA, USA

[b]Johns Hopkins University, Department of Computer Science, Baltimore, MD, USA

[c]Johns Hopkins University, Department of Electrical and Computer Engineering, Baltimore, MD, USA

[d]Johns Hopkins University, Department of Biomedical Engineering, Baltimore, MD, USA

ABSTRACT

Minimally invasive surgery carries the deadly risk of rupturing major blood vessels, such as the internal carotid arteries hidden by bone in endonasal transsphenoidal surgery. We propose a novel approach to surgical guidance that relies on photoacoustic-based vessel separation measurements to assess the extent of safety zones during these type of surgical procedures. This approach can be implemented with or without a robot or navigation system. To determine the accuracy of this approach, a custom phantom was designed and manufactured for modular placement of two 3.18-mm diameter vessel-mimicking targets separated by 10-20 mm. Photoacoustic images were acquired as the optical fiber was swept across the vessels in the absence and presence of teleoperation with a research da Vinci Surgical System. When the da Vinci was used, vessel positions were recorded based on the fiber position (calculated from the robot kinematics) that corresponded to an observed photoacoustic signal. In all cases, compounded photoacoustic data from a single sweep displayed the four vessel boundaries in one image. Amplitude- and coherence-based photoacoustic images were used to estimate vessel separations, resulting in 0.52-0.56 mm mean absolute errors, 0.66-0.71 mm root mean square errors, and 65-68% more accuracy compared to fiber position measurements obtained through the da Vinci robot kinematics. Results indicate that with further development, photoacoustic image-based measurements of anatomical landmarks could be a viable method for real-time path planning in multiple interventional photoacoustic applications.

1. INTRODUCTION

Surgeons often drill or make incisions in highly sensitive areas that contain critical blood vessels or nerves.[1,2] Two examples of surgeries that suffer from the lack of real-time visualization of critical nerves or blood vessels include mastoidectomies and endonasal transsphenoidal surgeries. In mastoidectomies, surgeons operate near the facial nerve with potential nerve damage leading to facial paralysis. As many as 79% of facial nerve ruptures caused in surgery go undiagnosed.[1] Endonasal transsphenoidal surgery also carries high risk if surgeons rupture either branch of the internal carotid artery while drilling through the sphenoid bone.[2] If injury to the carotid artery occurs, surgery to correct the arterial injury has 14% morbidity and 24-40% mortality rates.[3,4] Clear visualization of both branches of the artery could prevent ruptures from occuring during the drilling process.

These surgeries utilize intraoperative endoscopic camera images to visualize superficial anatomical structures and preoperative imaging modalities such as CT and MRI for guidance and navigation of subsurface anatomy.[5,6] However, the subsurface anatomy might not always match the preoperative images. While intraoperative CT imaging is an option,[7] it adds risk due to irradiation, adds cost, and has poor resolution.[8] Intraoperative MRI is also possible[9] and would not incur the radiation risks of CT, but the spatial resolution is similarly poor and the technique is more expensive.[8]

Our previous work shows that photoacoustic imaging can be used to visualize blood vessels through bone,[8] with extended potential to nerve visualization.[10,11] With this type of interventional imaging system, the alignment of the separated optical and acoustic hardware (i.e., optical fibers and ultrasound probes, respectively) can

*E-mail:mledijubell@jhu.edu

Photons Plus Ultrasound: Imaging and Sensing 2017, edited by Alexander A. Oraevsky, Lihong V. Wang, Proc. of SPIE Vol. 10064, 100642V · © 2017 SPIE · CCC code: 1605-7422/17/$18 · doi: 10.1117/12.2253532

potentially be controlled with a dedicated navigation system.[12] Our previous work also discusses the possible advantages of adding real-time photoacoustic imaging to improve accuracy, leading to a feasibility study demonstrating the potential of integrating photoacoustic imaging with the da Vinci Surgical System.[13] Although the previous work utilized synthetic photoacoustic images to illustrate this concept,[13] our vision is for the operator to use the console as in current procedures, with added information from simultaneous visualization of the endoscopic video and the real-time photoacoustic images.

The work presented herein is the first to investigate the ability of photoacoustic imaging to accurately quantify the separation between cylindrical targets such as blood vessels and nerves and thereby provide the surgeon with information about safe zones for operation, which can be implemented with or without a robot-held surgical tool or a dedicated navigation system. When a robot or navigation system is absent, guidance could be provided by attaching one or more optical fibers to the surgical tool and visualizing surgical tool tips simultaneously with critical anatomical features.[14] With a robot present (e.g., a teleoperated robot that controls a surgical tool and attached fiber), the robot-based tool tip coordinates can be obtained whenever a critical landmark appears in the photoacoustic image. We evaluate the accuracy of separation measurements obtained from both types of image-based measurements, as well as that obtained with both manual and teleoperated control of an optical fiber.

2. METHODS AND MATERIALS

2.1 Photoacoustic Imaging System

Our photoacoustic imaging system consisted of an Alpinion ECUBE 12R ultrasound system attached to an Alpinion L3-8 linear transducer (3-8 MHz bandwidth) and one of two lasers that were used in two separate experiments. One experiment used a portable Laser Components LS Series pulsed laser diode, and the second experiment utilized a larger Quantel Ultra100 Nd:YAG laser. For both lasers, the laser beam was directed through a 1-mm core diameter, 0.5 numerical aperture (NA) multimode optical fiber after coupling with an optical lens. Photoacoustic images were displayed in real-time during the experiments and the raw channel data was acquired for post-processing to determine vessel separation as described in Section 2.4.

The portable 905-nm wavelength pulsed laser diode was coupled to a collimator connected to a 1-mm core diameter, 0.5 NA optical fiber. The free end of the fiber was both attached to the tip of a teleoperated large needle driver da Vinci tool for teleoperation and detached for handheld (i.e., manual) control of the fiber. The pulse frequency was 40 Hz, the pulse length was 29 ns, and the peak power was 226 W, resulting in 0.6 μJ pulse energy from the laser module.

The 1064-nm wavelength laser beam from the Nd:YAG laser was focused through an aspheric lens coupled to the 1-mm core diameter, 0.5 NA optical fiber, which was manually operated and not attached to the da Vinci tool. The laser pulse repetition frequency was 20 Hz with a pulse length of 7 ns. The laser provided a trigger signal for the acquisition of photoacoustic data by the ultrasound system. The output laser beam from the optical fiber had pulse energy of 0.75 mJ.

2.2 Custom Modular Phantom

To test the image guidance method, we designed and built a custom phantom from laser cut acrylic, 3D printed components, and wooden stands for height adjustment of the inner container relative to the outer container. Guides for placement of blood vessels were positioned and secured via set screws and enabled modular placement of the vessels during experiments. Fig. 1 shows our phantom design with modularity in vessel separation provided by the movable vessel guides. This design builds on the phantom used in previous work, which consisted of inner and outer containers and was used to visualize *ex vivo* bovine blood in the presence of an *ex vivo* sheep brain and *ex vivo* human cadaver skull specimens.[15] Although these *ex vivo* tissues may be added to the current design, they were not included in this study in order to determine accuracy based on the best-case imaging scenario.

The phantom was filled with water to permit acoustic wave propagation. The ultrasound transducer was fixed against the acoustic window. A black, 3-mm diameter flexible rubber rod was used to mimic blood vessels. Two parallel blood vessels were placed in the phantom at four separation distances. The vessel separation was measured with calipers each time the vessel configuration was altered. This separation distance ranged from

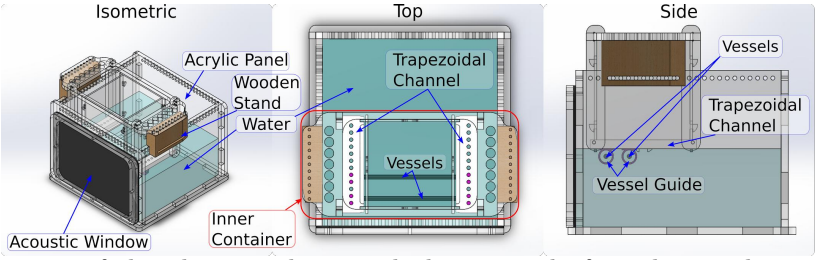

Figure 1: Overview of the phantom design, which consisted of acrylic panels, a rubber acoustic window for ultrasound signal reception, and plastic guides to control the vessel separation distances. The two parallel lines inside the phantom (top view) show a sample arrangement of parallel blood vessels. The phantom was filled with water for photoacoustic imaging.

10.06 mm to 20.14 mm for the three experiments, which is within the range of expected vessel separations during endonasal transsphenoidal surgery.[16] The ultrasound transducer was fixed in place relative to the acoustic window of the phantom. The optical fiber was pointed at the rubber targets, and could either be submerged in the water or maintained above the water line, as the bottom of the inner container was open to the water.

2.3 Fiber Sweeping Motion

In each trial, the fiber was positioned close to the acoustic window and swept away from it. Only the proximal and distal boundaries of the blood vessel are expected to be visible, due to factors such as constructive interference from subresolution optical absorbers on the target boundary, limited angle view with the linear array, and limited bandwidth of the transducer.[8,17] Thus, the goal of image acquisition was to see proximal and distal vessel boundaries rather than entire vessels. At each vessel boundary, the fiber was held in place while a photoacoustic image was acquired. For the teleoperated trials, the corresponding fiber and tool tip location (i.e. tracking data) was available from the da Vinci robot kinematics. Note that tracking information is not available for the manual trials.

There are two options for measuring vessel separation distances with the teleoperated system. The first option is based on the da Vinci tracking data, which can be acquired when the vessel boundary is visible in the photoacoustic image. The accuracy of this tracking-based method was determined by recording the two tool tip positions at which the two closest edges of the vessel boundaries were visible in real-time photoacoustic images

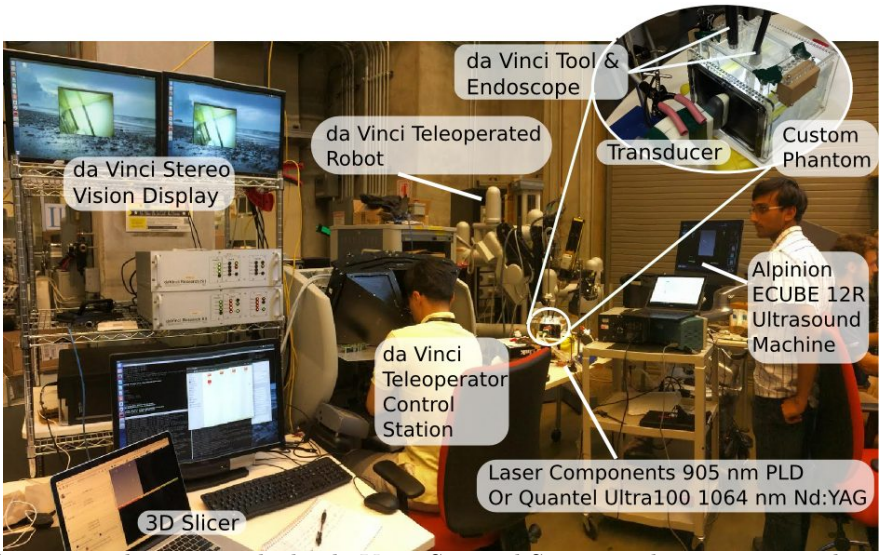

Figure 2: Physical setup used to test with the da Vinci Surgical System. The inset image shows the custom-built phantom.

(i.e., one edge per image). A second option is to determine the location of vessel boundaries in compounded photoacoustic images and use this image-based measurement to determine vessel separation distances. This second option can be applied in both manual and teleoperated trials.

Fig. 2 shows an image of the experimental setup when integrating our photoacoustic imaging system with the da Vinci Surgical System. Patient side manipulators are visible near the center of Fig. 2. The system is teleoperated from the master console. Videos from the da Vinci endoscopic camera manipulator were transferred to the master console and to the two monitors shown in the upper left corner of Fig. 2. Photoacoustic images were visible in real time on the screen of the ultrasound machine and not integrated with the master console, which is one end goal for a fully integrated system, as proposed in our previous publication.[13] The teleoperator used both the endoscopic video and the real-time photoacoustic video to position the tool tip.

Tracking data was collected by the 3D Slicer software installed on a separate laptop computer (shown in the bottom left of Fig. 2) through an OpenIGTLink connection with the da Vinci research software.[18] The upper right corner of Fig. 2 shows a close-up of our custom phantom. The ultrasound transducer was fixed to the acoustic window in the orientation shown using a passive arm. Alternatively, a custom mount can allow one of the da Vinci arms to support the transducer.[13] The optical fiber was attached to the da Vinci tool.

2.4 Data Analysis

Experiments were conducted with two parallel blood vessel-mimicking targets, and therefore four photoacoustic images were captured for every trial. These four images were post-processed to produce a single compounded image containing all vessel boundaries. This process is visually depicted in Fig. 3(a). Once a single compounded image was obtained, the brightest pixels in regions of interest surrounding vessel boundaries were identified. Vessel separation was determined by measuring the distance between the brightest pixels, as shown in Fig. 3(b). This distance was measured on images that were processed with both the more conventional amplitude-based delay-and-sum beamformer (DAS) and the relatively novel coherence-based short-lag spatial coherence (SLSC) beamformer (created with 8% of the receive aperture), which were both described and compared in our previous publication.[8] The SLSC beamformer was initially developed for ultrasound imaging,[19] translated to photoacoustic imaging,[20,21] and demonstrated to improve contrast when performing photoacoustic imaging with pulsed laser diodes,[22] which are notorious for their low power and poor image quality when utilizing conventional DAS imaging methods.

When using tracking data from the da Vinci surgical system, which provided an absolute position of the tool tip in three-dimensional space and therefore does not require any post-processing, vessel separation was calculated as the linear distance between two points in three-dimensional space:

$$\text{Distance} = \sqrt{(x_2 - x_1)^2 + (y_2 - y_1)^2 + (z_2 - z_1)^2}, \tag{1}$$

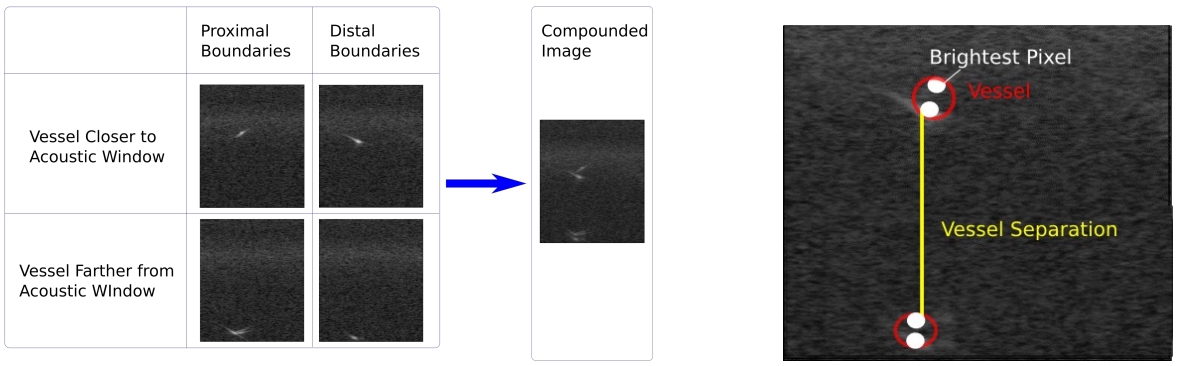

(a) (b)

Figure 3: (a) Four photoacoustic frames show the four different vessel boundaries from two vessels. These four frames were compounded in a single image. (b) The brightest pixel at each boundary in the compounded image was used to compute vessel separation.

where x, y, and z represent axes in three dimensional space, and the subscripts represent the indices of two independent points in space. Note that this measurement is affected by diffusion of the laser beam.

Distance measurements from the compounded photoacoustic image (illustrated in Fig. 3(b)) and from the da Vinci tracking data (provided by Eq. 1) were compared to the ground truth measured with calipers, and the absolute value of this deviation from this ground truth was displayed as box-and-whisker plots. Note that we are not using the ultrasound image as the ground truth because it is co-registered with the photoacoustic image. The horizontal line inside each box displays median error. The upper and lower edges of each box represent the first and third quartiles of the data set. The vertical lines connected to the boxes show the minimum and maximum values in each data set, excluding outliers, which are shown as plus symbols and defined as any value greater than 1.5 times the interquartile range.

The root-mean-square (RMS) error was computed across all trials and vessel separations for each type of data, as shown by Eq. 2:

$$\text{RMS Error} = \sqrt{\frac{\sum_{n=1}^{NVS}\left(\sum_{m=1}^{NVT_n} D^2\right)}{TNVT}} \tag{2}$$

where n is the trial number, NVS is number of vessel separations (four total), NVT is number of valid trials in a given vessel separation (at most ten), D is deviation from ground truth, and $TNVT$ is the total number of valid trials (at most forty). Note that several trials had to be excluded from data analysis calculations due to poor visualization of vessel boundaries in the compounded images.

The mean absolute error (MAE) was computed as shown in Eq. 3:

$$\text{MAE} = \frac{\sum_{n=1}^{NVS}\left(\sum_{m=1}^{NVT_n} |D|\right)}{TNVT} \tag{3}$$

3. RESULTS

An example from a single set of compounded data processed by the DAS and SLSC beamformers is shown in Fig. 4(a). Visualization of the targets is noticeably enhanced with the coherence-based SLSC image when compared to the amplitude-based DAS image. The intensity information as a function of depth for one line, located at lateral position 16.5 mm, is shown in Fig. 4(b). The four peaks in each line plot indicate one of the four vessel boundaries. Note that the intensity of the signal peaks in the SLSC image is generally greater than that of the DAS images, particularly in cases of low DAS peak amplitudes.

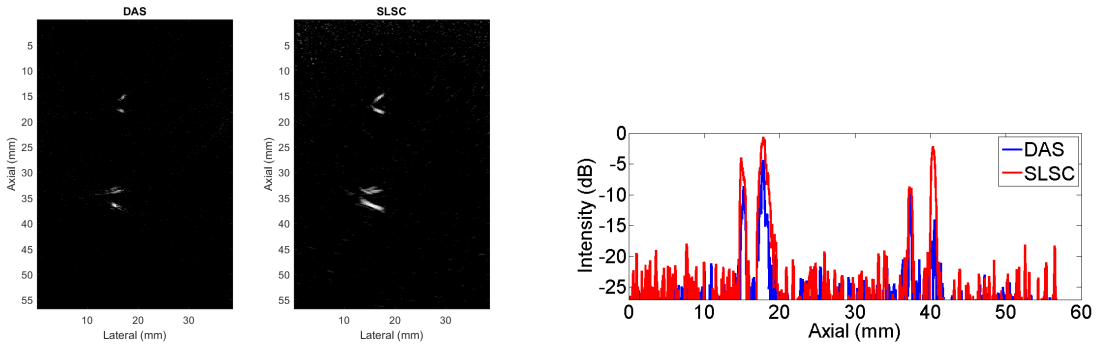

(a) (b)

Figure 4: (a) The amplitude-based DAS image shows all four vessel boundaries acquired with the pulsed laser diode. Visualization of the targets is noticeably enhanced with the coherence-based SLSC image. Both images are displayed with 20 dB dynamic range. (b) Line plots through the same lateral location (16.5 mm) with the four peaks indicating one of the four vessel boundaries. The intensity of the peaks in the SLSC images is generally greater than that of the DAS images, particularly in cases of low DAS peak amplitudes.

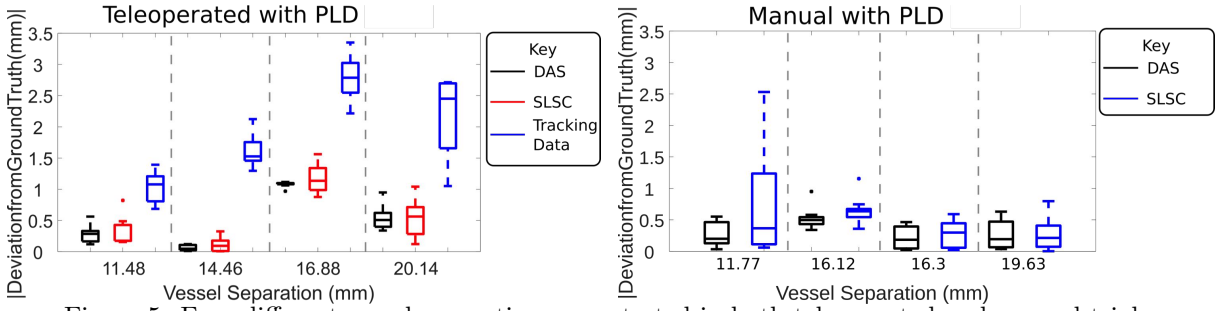

Figure 5: Four different vessel separations were tested in both teleoperated and manual trials.

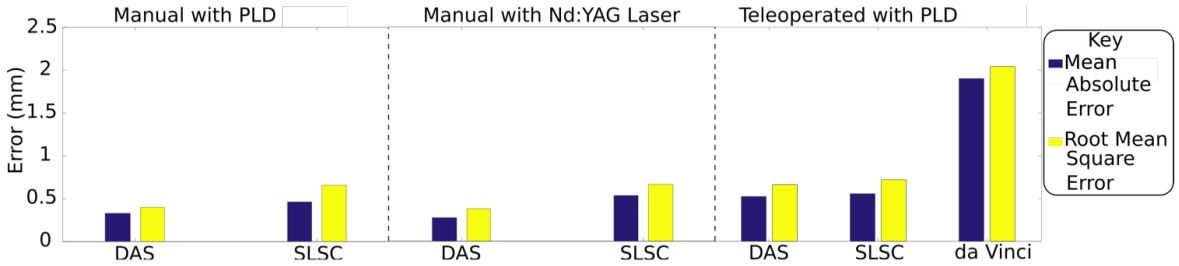

Figure 6: Summary of MAE and RMS error for the three experiments.

Fig. 5 shows results from experiments with the optical fiber coupled to the pulsed laser diode and attached to the da Vinci tool tip. For the tracking-based separation measurements obtained in the teleoperated trials, there is an apparent increase in the deviation from ground truth values as the vessel separation distance increases, particularly for separation distances ranging from 11.48 mm to 16.88 mm. Each DAS and SLSC photoacoustic image generally provides more accurate and precise estimation of vessel separation when compared to measurements obtained with the da Vinci tracking results. Similar accuracy for the image-based measurements were observed with a manually operated optical fiber (i.e., no assistance from the da Vinci robot).

When comparing RMS error, the SLSC beamformer provides a 64.78% improvement in accuracy compared to the tracking data, while the DAS beamformer provides a 67.56% improvement in accuracy compared to the tracking data, as demonstrated in Fig. 6. The RMS error for the tracking data is 2.04 mm. Similar improvements in accuracy (70.74% and 72.47%, respectively) were observed when considering the MAE, which was 1.90 mm for the tracking data, as illustrated in Fig. 6.

For the data analysis method chosen here (i.e., evaluations based on the brightest pixels), DAS images generally provided higher accuracy and precision relative to SLSC images, particularly when imaging with the Nd:YAG laser. However, SLSC images resulted in 45% less trials excluded from data analysis calculations due to poor visualization of vessel boundaries in the compounded images (i.e., the total number of trials excluded for every vessel separation tested was 11 out of 40 trials for DAS vs. 6 out of 40 trials for SLSC). The majority of these excluded trials were from experiments with the pulsed laser diode rather than the Nd:YAG laser, likely due to the lower energy (6.6 μJ vs. 0.75 mJ), which decreases photoacoustic signal-to-noise ratios.

4. DISCUSSION

We demonstrated that real-time photoacoustic imaging may be integrated with a da Vinci Surgical System with sufficient accuracy to determine the distance between sensitive anatomical landmarks (e.g., blood vessels or potentially nerves) separated by ~1-2 cm during minimally invasive surgeries. Results indicate that the proposed photoacoustic image guidance provides sub-millimeter MAE and RMS errors when determining this separation, thus providing the potential to maximize surgical workspace while minimizing damage. In general, separation measurements are important to provide the surgeon with information about safety zones for operation. When provided in the absence of a robot (i.e., manual operation of the optical fiber), this information is only available

in the image coordinate system, and does not require calibration or a dedicated navigation system as proposed in our previous work.[12] When this information is provided with the fiber attached to a teleoperated robot, the separation distances can be displayed in both the image coordinate system and the robot coordinate system, assuming calibration of the ultrasound probe and optical fiber to the robot coordinate system.

Image-based vessel separation calculations were performed with DAS and SLSC images, which both produced more accurate results than using the da Vinci tracking data. Although the image-based measurements require additional post processing when compared to tracking-based measurements, the increase in accuracy substantiates the additional time and computational expense required to perform image-based measurements. DAS images generally provided greater accuracy than SLSC images because the data analysis was biased toward amplitude information, while SLSC images are known to be independent of signal amplitude. However, the SLSC images increased target visibility, resulting in fewer trials excluded from the final calculations, representing a trade-off between using SLSC images for image visualization and DAS images for amplitude-based data analyses. For real-time guidance, SLSC imaging would likely be more beneficial due to the higher contrast images.

There are multiple clinical implications when integrating the proposed photoacoustic image guidance system into existing surgical workflows. First, the proposed sweeping motion and associated separation measurements can provide the surgeon with assurance regarding the extent of available workspace when the optical fiber is either manually operated or teleoperated (assuming that there is enough room to visualize two critical structures in one sweep). Second, the photoacoustic system can be developed to provide indications about where to drill (or where not to drill), as the presence of a vessel boundary would indicate that the surgeon should change the direction of drilling, and the absence of a vessel boundary would indicate that the surgeon is operating in a safety zone (assuming that the ultrasound probe is correctly positioned to visualize the region of interest). An additional assumption when bone is present is that the bone is thin enough for photoacoustic imaging.[14] Third, with the additional integration of the robotic system, the surgeon would have quantitative information about the center of safety zone in the robot coordinate system. This integration is advantageous because the surgeon can obtain information about the vessel locations with respect to the robot-held surgical tool (which would be attached to one or more optical fibers). Similar information may be obtained with the image-based coordinate system if features such as the tool tip are also visible in the photoacoustic image.[14]

5. CONCLUSION

To the authors' knowledge, this work is the first to demonstrate that the distance between critical anatomical features such as blood vessels and nerves can be estimated with photoacoustic imaging to provide reasonable accuracy for surgical guidance. This novel image-based guidance method can be combined with robots such as the da Vinci surgical system and is a feasible alternative or adjunct to existing imaging modalities such as CT and MRI. The ability to clearly visualize hidden vessels and nerves with real-time photoacoustic imaging can reduce the incidence of morbidity and mortality in a wide range of minimally invasive surgeries, including endonasal transsphenoidal surgery and otological surgery (e.g., mastoidectomies). In telerobotic operations, the addition of real-time photoacoustic image guidance improves the accuracy of separation measurements when compared to the tool position tracking information provided by the robot kinematics. Results are promising for real-time path planning in both robotic and nonrobotic interventional photoacoustic applications.

Acknowledgements

This work was completed in partnership with the NSF Computational Sensing and Medical Robotics Research Experience for Undergraduates program. Funding was provided by NSF Grants EEC-1460674 and NRI-1208540, and NIH Grants K99-EB018994 and R00-EB018994. The authors thank Anton Deguet, Blackberrie Eddins, Sathappan Ramesh, Youri Tan, Joshua Wang, and Zerui Wang for their assistance.

REFERENCES

[1] J. D. Green, C. Shelton, and D. E. Brackmann. Iatrogenic facial nerve injury during otologic surgery. *The Laryngoscope*, 104(8):922–926, 1994.

[2] G. R. Isolan, P. H. P. de Aguiar, E. R. Laws, A. C. P. Strapasson, and O. Piltcher. The implications of microsurgical anatomy for surgical approaches to the sellar region. *Pituitary*, 12(4):360–367, 2009.

[3] M. Perry, W. Snyder, and E. Thal. Carotid artery injuries caused by blunt trauma. *Annals of Surgery*, 192(1):74, 1980.

[4] J. Raymond, J. Hardy, R. Czepko, and D. Roy. Arterial injuries in transsphenoidal surgery for pituitary adenoma; the role of angiography and endovascular treatment. *American Journal of Neuroradiology*, 18(4):655–665, 1997.

[5] H. Lim, N. Matsumoto, B. Cho, J. Hong, M. Yamashita, M. Hashizume, and B.-J. Yi. Semi-manual mastoidectomy assisted by human–robot collaborative control–a temporal bone replica study. *Auris Nasus Larynx*, 43(2):161–165, 2016.

[6] Y. Cao, J. Hui, A. Kole, P. Wang, Q. Yu, W. Chen, M. Sturek, and J.-X. Cheng. High-sensitivity intravascular photoacoustic imaging of lipid–laden plaque with a collinear catheter design. *Scientific Reports*, 6, 2016.

[7] K. Kitazawa, H. Okudera, T. Takemae, and S. Kobayashi. [ct guided transsphenoidal surgery: report of nine cases]. *No shinkei geka. Neurological surgery*, 21(2):147–152, 1993.

[8] M. A. L. Bell, A. K. Ostrowski, K. Li, P. Kazanzides, and E. M. Boctor. Localization of transcranial targets for photoacoustic-guided endonasal surgeries. *Photoacoustics*, 3(2):78–87, 2015.

[9] T. H. Schwartz, P. E. Stieg, and V. K. Anand. Endoscopic transsphenoidal pituitary surgery with intraoperative magnetic resonance imaging. *Neurosurgery*, 58(1):ONS–44, 2006.

[10] R. Li, E. Phillips, P. Wang, C. J. Goergen, and J.-X. Cheng. Label-free in vivo imaging of peripheral nerve by multispectral photoacoustic tomography. *Journal of Biophotonics*, 9(1-2):124–128, 2016.

[11] J. M. Mari, S. West, P. C. Beard, and A. E. Desjardins. Multispectral photoacoustic imaging of nerves with a clinical ultrasound system. In *SPIE BiOS*, pages 89430W–89430W. International Society for Optics and Photonics, 2014.

[12] S. Kim, H. J. Kang, A. Cheng, M. A. L. Bell, E. Boctor, and P. Kazanzides. Photoacoustic image guidance for robot-assisted skull base surgery. In *2015 IEEE International Conference on Robotics and Automation (ICRA)*, pages 592–597. IEEE, 2015.

[13] S. Kim, Y. Tan, P. Kazanzides, and M. A. L. Bell. Feasibility of photoacoustic image guidance for telerobotic endonasal transsphenoidal surgery. In *2016 IEEE International Conference on Biomedical Robotics and Biomechatronics*. IEEE, 2016.

[14] B. Eddins and M. A. L. Bell. Design of a multifiber light delivery system for photoacoustic-guided surgery. *Journal of Biomedical Optics*, 22(4), 2017.

[15] M. A. L. Bell, A. B. Dagle, P. Kazanzides, and E. M. Boctor. Experimental assessment of energy requirements and tool tip visibility for photoacoustic-guided endonasal surgery. In *SPIE BiOS*, pages 97080D–97080D. International Society for Optics and Photonics, 2016.

[16] W. H. Renn and A. L. Rhoton Jr. Microsurgical anatomy of the sellar region. *Journal of Neurosurgery*, 43(3):288–298, 1975.

[17] Z. Guo, L. Li, and L. V. Wang. On the speckle-free nature of photoacoustic tomography. *Medical Physics*, 36(9):4084–4088, 2009.

[18] P. Kazanzides, Z. Chen, A. Deguet, G. S. Fischer, R. H. Taylor, and S. P. DiMaio. An open-source research kit for the da Vinci® Surgical System. In *2014 IEEE International Conference on Robotics and Automation (ICRA)*, pages 6434–6439. IEEE, 2014.

[19] M. A. Lediju, G. E. Trahey, B. C. Byram, and J. J. Dahl. Short-lag spatial coherence of backscattered echoes: Imaging characteristics. *IEEE Transactions on Ultrasonics, Ferroelectrics, and Frequency Control*, 58(7):1377–1388, 2011.

[20] B. Pourebrahimi, S. Yoon, D. Dopsa, and M. C. Kolios. Improving the quality of photoacoustic images using the short-lag spatial coherence imaging technique. In *SPIE BiOS*, pages 85813Y–85813Y. International Society for Optics and Photonics, 2013.

[21] M. A. L. Bell, N. Kuo, D. Y. Song, and E. M. Boctor. Short-lag spatial coherence beamforming of photoacoustic images for enhanced visualization of prostate brachytherapy seeds. *Biomedical Optics Express*, 4(10):1964–1977, 2013.

[22] M. A. L. Bell, X. Guo, H. J. Kang, and E. Boctor. Improved contrast in laser-diode-based photoacoustic images with short-lag spatial coherence beamforming. In *2014 IEEE International Ultrasonics Symposium*, pages 37–40. IEEE, 2014.